Predicting the steady-state isochronal stratigraphy of ice shelves using observations and modeling

Vjeran Višnjević[1], Reinhard Drews[1], Clemens Schannwell[2], Inka Koch[1], Steven Franke[3], Daniela Jansen[3], and Olaf Eisen[3,4]

[1]Department for Geoscience, University of Tübingen, Tübingen, Germany
[2]Max Planck Institute for Meteorology, Hamburg, Germany
[3]Alfred Wegener Institute, Helmholtz Centre for Polar and Marine Research, Bremerhaven, Germany
[4]University of Bremen, Bremen, Germany

Correspondence: Vjeran Višnjević (vjeran.visnjevic@uni-tuebingen.de)

Abstract. Ice shelves surrounding the Antarctic perimeter ~~decelerate~~ moderate ice discharge towards the ocean through buttressing. Ice-shelf evolution and integrity depend on the local surface accumulation, basal melting and on the spatially variable ice-shelf viscosity. These ~~parameters~~ components of ice shelf mass balance are often poorly constrained by observations and introduce uncertainties in ice-sheet projections~~for the ice-sheet evolution~~. Isochronal radar stratigraphy is an observational archive for the atmospheric, oceanographic and ice-flow history of ice shelves~~with potential to assist model calibration~~. Here, we ~~explore the possibility of using a simple and observationally driven ice-flow forward model to predict the ice-shelf stratigraphy~~ predict the stratigraphy of locally accumulated ice on ice shelves with a kinematic forward model for a given ~~atmospheric-~~ atmospheric and oceanographic scenario. ~~We validate this approach~~ This delineates the boundary between local meteoric ice (LMI) and continental meteoric ice (CMI). A large LMI to CMI ratio hereby marks ice shelves whose buttressing strength is more sensitive to changes in atmospheric precipitation patterns. A mismatch between the steady-state predictions of the kinematic forward model and observations from radar can highlight inconsistencies in the atmospheric- and oceanographic input data, or be an indicator for a transient ice-shelf history not accounted for in the model. We discuss pitfalls in numerical diffusion when calculating the age field and validate the kinematic model with the full Stokes ice-flow model Elmer/Ice~~and present a test case for the~~. The Roi Baudouin Ice Shelf (East Antarctica) ~~, where we compare model predictions with radar observations . The presented method enables us to investigate whether ice shelves are in steady-state and to delineate how much of the ice-shelf volume is determined by its~~ serves as a test case for this approach. There, we find a significant East-West gradient in the LMI/CMI ratio. The steady-state predictions concur with observations on larger-spatial scales (> 10 km), but deviations on smaller scales are significant (e.g., because local surface accumulation ~~. This can be used to better understand variability in~~ patterns near the grounding zone are underestimated in Antarctic-wide estimates). Future studies can use these mismatches to optimize the input data, or to pinpoint transient signatures in the ice-shelf ~~rheology and for estimations which ice shelves are particularly susceptible to changes of surface accumulation rates in the future. Moreover, the numerically efficient prediction of isochronal stratigraphy is a step forward towards integrating radar data into ice-flow models using inverse methods. This has potential to constrain ocean-induced melting beneath Antarctic ice shelves using the ever-growing~~ history using the ever growing archive of radar observations of internal ice stratigraphy.

1 Introduction

The Antarctic Ice Sheet holds a ~~sea-level equivalent of~~ sea level equivalent ice volume of ca. 58 m of global sea level rise (Fretwell et al., 2013; Morlighem et al., 2020)~~and some studies suggest a sea level contribution~~ , with maximum estimates of up to 40 cm by the end of this century (Levermann et al., 2020; Edwards et al., 2021). Forming at the outlets of the ice/ocean boundary surrounding Antarctica, ice shelves play a major role in these future projections due to their buttressing effect on glacier flow (Fürst et al., 2016). The stability of ice shelves has been a focus of many studies (Rignot et al., 2008; Jansen et al., 2010; Gudmundsson, 2013; Alley et al., 2016; Fürst et al., 2016; Banwell, 2017; Schannwell et al., 2018), and predicting their future behavior requires understanding the impact of future changes in atmospheric and oceanic forcing on their structural integrity. Uncertainties in ice shelf evolution are in part due to an insufficient understanding of the processes which drive ocean-induced melting at the grounding-line and further seawards. The internal ice-shelf stratigraphy, as imaged by radar, is an underexplored archive which can be used to better constrain model predictions.

In grounded ice, ~~the geometry of isochronal radar reflection horizons has been used in numerous studies in conjunction with ice-flow modeling to unravel ice dynamics (Nereson et al., 1998, 2000; Nereson and Waddington, 2002; Hindmarsh et al., 2009; Waddingt~~ ~~, or surface accumulation history (Waddington et al., 2007; Lenaerts et al., 2014, 2019; Pratap et al., 2021)~~ numerous localized studies have used radar observations to infer surface and basal accumulation history (Nereson et al., 1998, 2000; Nereson and Waddington, of various sectors in ~~Antarctica or Greenland . This approach also gives insight~~ Greenland or Antarctica. These approaches also gave insights into dynamic processes, e.g., such as basal sliding (Holschuh et al., 2017) and englacial folding (Bons et al., 2016; Jansen et al., 2016). Recent studies have focused on using the geometry of isochronal radar reflection horizons to reconstruct the ice dynamics of mountain glaciers (Jouvet et al., 2020), and also on a continental scale in Greenland (Born and Robinson, 2021) and Antarctica (Sutter et al., 2021). In ice shelves, similar concepts have been applied to derive the surface accumulation (e.g., Pratap et al., 2021) and basal melt rates (Pattyn et al., 2012; Matsuoka et al., 2012; Das et al., 2020). The internal radar stratigraphy also holds information with respect to the ice shelf's dynamic history and internal structure (Das et al., 2020), but this has been less often exploited so far.

~~In this study, we use ice shelf surface velocities derived by remote sensing to approximate a 3D velocity field of the ice shelf using a simple kinematic ice flow forward model. With this, we can predict the ice-shelf stratigraphy~~ Here, we predict the age stratigraphy of locally accumulated ice on ice shelves for a given set of oceanic and atmospheric boundary conditions~~and compare this to radar observations. One outcome is the delineation of two distinct ice bodies, namely ice that is formed~~ . The meteoric ice orignating from the grounded part of the ice sheet is overlaid by the ice originating from local accumulation ~~seawards of the grounding line, and ice that is advected from upstream of the grounding line~~on the ice shelf. Consistent with previous publications (Das et al., 2020), we refer to these two ice bodies as ~~continental~~ local meteoric ice (~~CMI) and local~~ LMI) and continental meteoric ice (~~LMI~~CMI). The implications of the LMI/CMI ratio of a particular ice shelf are twofold: First, the two ice bodies can have different rheological properties because CMI, deposited further upstream, may contain colder and stiffer ice that protrudes into the ice shelves from their tributary ice streams (Larour et al., 2005; Khazendar et al., 2011). This ice may also ~~be imprinted in terms of crystal orientation fabric from its source region~~

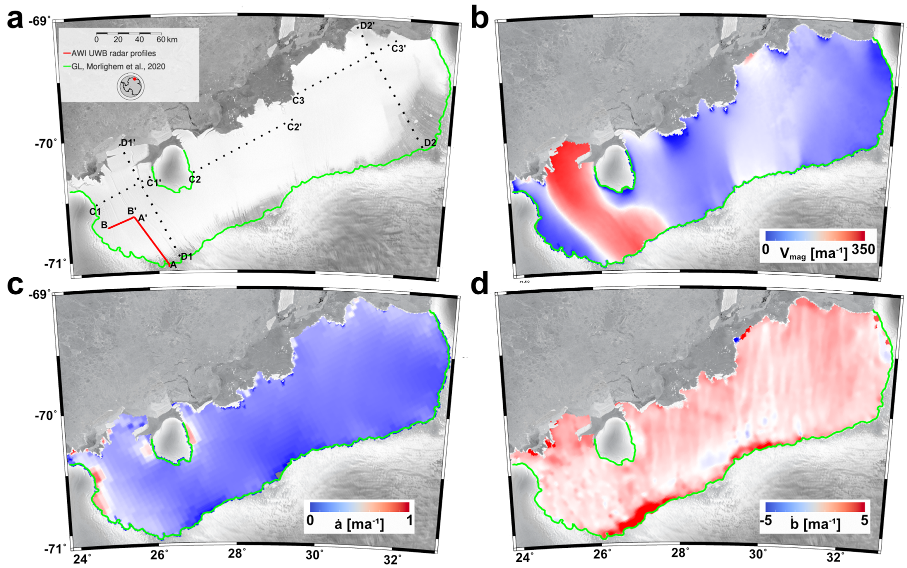

Figure 1. a) Overview of the Roi Baudouin Ice Shelf located in Dronning Maud Land, East Antarctica. The grounding line (Morlighem et al., 2020) is marked in green and radar profile lines, ~~A-A~~A–A’ and ~~B-B~~B–B’, used for validation are located in red. Black dotted lines C1, C2, ~~and~~ C3, D1, and D2 correspond to the profiles shown in ~~Fig~~Figs. 5 and 6. The ~~Radarsat~~ RADARSAT Mosaic (Jezek, 2003) is shown in the background. (b) Surface speed (Gardner et al., 2018, 2019), (c) ~~Surface~~ surface accumulation rate (positive for mass gain, Lenaerts et al. (2014)), (d) ~~Basal melting rate~~ basal melt rates (positive for mass loss, Adusumilli et al., 2020).

~~(e.g., Alley, 1992; Thomas et al., 2021)~~show stronger orientation fabric because of stress-strain configurations experienced during flow (e.g., Alley, 1992; Thomas et al., 2021), whereas the LMI will not. Second, ice shelves that contain a large fraction of LMI are more susceptible to changes in atmospheric precipitation compared to ice shelves which are predominantly sustained by their tributary ice streams. This is relevant for future ice-shelf stability because some predictions suggest a stable or even decreasing surface accumulation for ice shelves in contrast to the overall predicted increase for the rest of the Antarctic continent (Kittel et al., 2021). In the following, we present details about the kinematic forward model (Sect. 2.1), its validation (Sect. 2.2) including numerical uncertainties (Sect. 2.3). We then model the steady-state LMI stratigraphy of the Roi Baudouin Ice Shelf and compare the predictions with radar observations (Sect 2.4). We interpret differences between observations and predictions in terms of flawed input data (oceanic, climatic) and/or transient signatures.

2 Methods

The governing equation to predict the ice stratigraphy is the advective age equation:

$$\frac{\partial A}{\partial t} + \mathbf{v} \cdot \nabla A = 1. \tag{1}$$

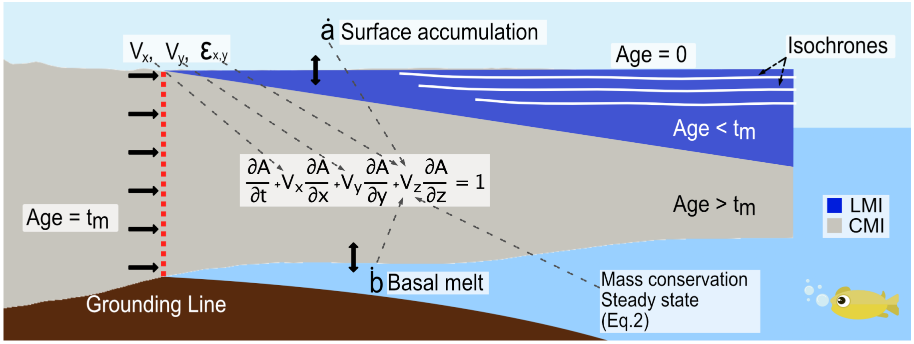

Figure 2. ~~Scheme~~ Illustration of the idealized ice shelf representing the distinction between the local meteoric ice (LMI, blue) and the continental meteoric ice advected from the ice sheet (CMI, gray). Isochrones are calculated by solving ~~(~~Eq. 1~~)~~, using observed horizontal velocities (V_x, V_y) and derived vertical velocities including fixed surface accumulation and basal ~~melt rate~~ melt-rate fields (Eq. 2). On the inflow boundary upstream of the grounding line the age of ice is set to the length of the simulation time (t_m).

The age of ice A at depth z is given by aging (i.e., the source term on the right-hand side) and ice advection, where $\mathbf{v}$ is the ice velocity (V_x, V_y, V_z). Contours of the age field provide a natural comparison to the isochronal radar observations. ~~The two main challenges in implementing this approach are (1)dealing with numerical diffusion, and (2)prescribing the three-dimensional velocity field~~In the following, we derive the required 3D velocities from the surface velocities assuming plug-flow (i.e., the shallow shelf assumption (SSA), Morland, 1987; MacAyeal, 1989; Weis et al., 1999, sec. 2.1). We validate this assumption using the full Stokes model Elmer/Ice in a synthetic geometry (referred to as MISMIP EXP1 originating from the setup from Pattyn et al. (2012), sec 2.2). Numerical diffusion in ~~classical discretization schemes can be minimized (e.g., Greve et al., 2002) but not fully avoided unless other approaches such as tracking the deformation in time and not space are implemented (Born, 2017; Born and Robinson, 2021). We will quantify the degree of diffusion by comparing the numerical predictions with analytical solutions for a specific~~ the solution of Eq. 1 is quantified with another test case (~~Sect~~referred to as NumDiff experiment) where an analytical solution exists (sec. 2.3~~, 3.2). The velocities required for Eq. (1) are often modeled and as such include all the uncertainties typical for ice-flow modelling, e.g., uncertainties in the Glen flow index (Bons et al., 2016) or the ice softness parameter (**?**). We circumvent this step by assuming the flow regime of ice shelves where the horizontal velocities do not significantly change with depth (i.e., the shallow shelf assumption (SSA), Morland, 1987; MacAyeal, 1989; . We illustrate this in the following sections.~~). We then apply this method to the Roi Baudouin Ice Shelf (referred to as RBIS experiment) where radar data are available.

2.1 Prediction of ice-shelf stratigraphy with observed surface velocities

~~We adopt a coordinate system such that $z = 0$ corresponds with the ice surface and z increases with depth. The x- and y-directions correspond with the along- and across-flow direction, respectively. The horizontal velocities at the surface (V_x, V_y) are obtained from observations and due to negligible basal friction these change little with depth. In steady state, this enables~~

~~the analytical derivation of the vertical velocities (Drews et al., 2020) as a function of the local~~ Vertical ice-flow velocities are derived from observed surface velocities (Drews et al., 2020) ice thickness H, the surface strain rates, the surface accumulation rate ($\dot{a}$, positive for mass gain), and the basal melt rate ($\dot{b}$, positive for mass loss):

$$V_z = \frac{\rho_i}{\rho_w}\dot{a} + (1-\frac{\rho_i}{\rho_w})\dot{b} + [H(1-\frac{\rho_i}{\rho_w}) + z]\nabla\cdot\mathbf{V_H} \tag{2}$$

where ρ_i and ρ_w are the respective densities of ice and water, and V_H is a vector containing horizontal surface velocities. We adopt a coordinate system such that $z = 0$ corresponds to the ice surface and z increases with depth. The x- and y-directions correspond to the along- and across-flow direction, respectively. The horizontal velocities at the surface (V_x, V_y) are obtained from observations and it is assumed that they do not change with depth (i.e. plug flow), which is very well justified for ice shelves. With the three-dimensional velocity field at hand, Eq. (1) is solved numerically using the open source finite element library Elmer/Ice (Gagliardini et al., 2013). Velocity gradients are calculated using the strain rate solver in Elmer, and a separate solver is written to pass the vertical velocities from Eq. (2) to the age solver.

The age solver solves Eq. (1) with a semi-Lagrangian scheme (Martín and Gudmundsson, 2012). We set $A(z=0)$ = 0, assuming that there is no ablation at the ice surface (Fig 2). Due to a lack of observational age constraints at the grounding line, the age is initialized with 0 seawards of the grounding line. Upstream thereof, the age is initialized with the ~~simulation runtime~~ total runtime of the experiment, t_m. These initial conditions provide an easy way to delineate the CMI-LMI boundary by finding the line $A = t_m$. ~~Although convenient, such choice of initial~~ These boundary conditions leads to a kink in the age-depth profiles at the contact point between LMI and CMI. This cannot adequately be captured with the semi-Lagrangian tracing scheme and deviations from the analytical and numerical schemes will be particularly evident around this transition (Sect. 3.2).

The results are verified by comparing the predicted isochrone stratigraphy with radar-observed internal layering (~~A-A', B-B~~A–A', B–B'; Fig. 1)~~which are typically considered to also be isochronous (e.g., Winter et al., 2019).~~ . The age of radar isochrones is often unknown, and consequently we can only compare spatial patterns and not absolute magnitudes. For the comparison of model results and observations, we contour the modelled age–depth field and choose a predicted isochrone with the same mean depth as the observed one (e.g., Nereson et al., 1998). Post-processing of the modeled age fields is done in Paraview (Henderson, 2004).

Steady-state conditions are assumed throughout. ~~The~~ For the real-world test case scenario of the Roi Baudouin Ice Shelf (referred to as RBIS experiment), the ice-shelf geometry is obtained from BedMachine Antarctica (Morlighem et al., 2020), horizontal surface velocities are taken from satellite observations (Gardner et al., 2018, 2019), the surface accumulation rate from RACMO 3.5 (Lenaerts et al., 2014), and the basal melt rate from a compilation of satellite derived surface height and velocity data combined with a firn layer model (Adusumilli et al., 2020). Those pan-Antarctic input data sets were chosen to enable ~~later~~ an expansion of the applied methodology to all Antarctic ice shelves ~~. For the test-case of the Roi Baudouin Ice Shelf, the continental products were cross-checked with the available higher resolution local products (Berger et al., 2017).~~

~~Simulations are run with~~ at a later stage. We run the simulations for 500 years, with 100 vertical layers, ~~with~~ a horizontal resolution of 1km and a time step of 0.1 year. The computation time (wallclock time) for a single simulation using 100 ~~partitions~~

CPUs (Central Processing Units) on 5 ~~Nodes is 22 h~~ nodes is 22h on a cluster with Intel Xeon E5-2630 processors. Prior to the real-world test case scenario we first validate the kinematic velocities and quantify numerical diffusion. Both is done for the cases with synthetic geometries.

2.2 Validation of derived velocities~~with a synthetic 3D full Stokes model~~

Because Eq. (2) only holds in areas where the shallow-shelf assumption is valid, the ~~analytical derivations are cross-checked~~ validity of the analytical formula is tested in a synthetic ~~case~~ experiment with an isothermal, isotropic, 2D, full Stokes model implemented in Elmer/Ice (Gagliardini et al., 2013). The model setup strictly follows the geometry and parameters used in the ~~Stdn~~ MISMIP EXP 1 experiment in the marine ice-sheet modeling intercomparison project ~~(Pattyn et al., 2012), only with~~ (Pattyn et al., 2012), with the exception of a reduced ice shelf length (500 km), $\dot{a}$ = 0.3 ma^{-1} and $\dot{b}$ = 0 ma^{-1} (assuming a constant density of 917 kgm^{-3}), and the grounding line condition set to first floating (Gagliardini et al., 2013). The model is initialized close to a steady state geometry ~~and is run~~ from the EXP1 experiment (Pattyn et al., 2012) and evolves to a steady-state over 2500 years. Twenty vertical layers are used (corresponding to a mean spacing of around 20 m) and linearly increasing element spacing in the horizontal, ranging from less than 10 m near the grounding line up to 10 km towards the terminus. The modeled horizontal velocities are then used to derive vertical velocities using Eq. (2) and are compared to the ~~FS~~ full-Stokes vertical velocity calculated by Elmer/Ice. This comparison naturally highlights areas such as the grounding zone where the SSA assumptions of depth-invariable horizontal flow are violated, and the differences compared to the ~~FS~~ full-Stokes solution are the largest.

2.3 Quantification of numerical diffusion

~~The degree of diffusion is quantified as a function of the number of vertical layers (N_z). Predictions are compared to an analytical solution of A(x, z) and the linked LMI/CMI boundary. This is done by considering an unbuttressed,~~ In order to quantify numerical diffusion, we consider another time-invariant~~($\frac{\partial A}{\partial t}$ = 0 in Eq. 1), two-dimensional ice shelf~~, unbuttressed, 2D, slab of ice with constant and depth-invariant horizontal velocities ~~. In that case the vertical velocity is also constant so that~~ (Fig. 4). Consequently the vertical velocities are also constant and the trajectory along the LMI/CMI boundary $z_{DL}(x)$ of a particle deposited at the grounding line (GL) reduces to:

$$z_{DL}(x) = -\frac{V_z}{V_x}(x - x(GL)), \text{for } x > x(GL). \tag{3}$$

The corresponding age field in the LMI body therefore increases linearly with depth:

$$A(x,z) = -\frac{z}{V_z}, \text{ for } z < z(LMI), \tag{4}$$

and is constant with depth for the CMI body:

Table 1. ~~*Parameters used in 2D synthetic ice shelf test Section 2.3*~~*Parameters used in NumDiff experiment Section 2.3*

	Constants	Value	Units
Lx	Length of Domain	60	km
$\mathrm{N_x}$	Number of points in x	1269	
$\mathrm{N_z}$	Number of vertical layers	10/25/50/100/200	
Time	Simulation time	300	a
$\mathrm{V_x}$	Horizontal Velocity	200	$\mathrm{ma^{-1}}$
$\mathrm{V_z}$	Vertical Velocity	1	$\mathrm{ma^{-1}}$

$$A(x,z) = \frac{A_0 V_z + V_z\big(x - x(GL)\big)}{V_x V_z}, \text{ for } z > z(LMI). \tag{5}$$

We refer to this test case as NumDiff experiment. The LMI/CMI boundary ~~for more general velocity fields~~ can also be obtained ~~from streamline tracing and here~~ independent from the Age equation using streamline tracing starting at the grounding line. Here, this is done ~~with an implementation from~~ as additional validation for the LMI/CMI boundary using second order Runge-Kutta tracing scheme implemented in Paraview (Fig. 4). The effect of numerical diffusion is illustrated as a function of number of vertical layers by comparing the predicted age-depth structure with the analytical solutions of Eqs 4 and 5.

2.4 Radar observation and validation site of the Roi Baudouin Ice Shelf

The Roi Baudouin Ice Shelf is located in a comparatively narrow ice-shelf belt surrounding coastal Dronning Maud Land, East Antarctica. This ice shelf is well suited to demonstrate the feasibility of our approach as previous studies in that area have quantified the surface accumulation rates (Lenaerts et al., 2014) and basal melt rates (Berger et al., 2017) at comparatively high resolution including ground-truth data. Moreover, analysis of the radar stratigraphy across ice rises (Drews, 2015; Callens et al., 2016) in that area indicates that the entire catchment is likely to have been close to steady-state for the last several decades. The ice shelf is dissected with numerous ice shelf channels which are located in areas in which our model assumptions of depth-invariant horizontal velocities are likely violated (Drews, 2015; Drews et al., 2020; Wearing et al., 2021).

The radar data used in this study were collected with AWI's (Alfred Wegener Institute, Helmholtz Centre for Polar and Marine Research) multichannel ultra-wideband ~~(UWB)~~ radar system (Rodriguez-Morales et al., 2014; Hale et al., 2016) in the austral summer 2018/19 using the eight-element radar system which is installed on AWI's Polar 6 BT-67 aircraft. Data were recorded in a frequency range of 150-520 MHz at an altitude of 365 m above ground. For radar data processing, which comprises of pulse compression, synthetic aperture radar focusing, and array processing ~~(for details, see Rodriguez-Morales et al., 2014; Franke~~ (Rodriguez-Morales et al., 2014; Franke et al., 2020), we used the CReSIS Toolbox ~~(CReSIS, 2020)~~(CReSIS, 2020). The synthetic aperture radar processing was ~~optimised~~ optimized to increase the sensitivity of larger angle returns to achieve a better resolution of steeply inclined internal reflectors ~~(Franke et al., 2021)~~(Franke et al., 2022). The final radargrams have a range resolution of 0.35 m and a trace spacing of 6 m.

~~Internal radar~~ Radar internal reflection horizons (~~i.e., isochronal surfaces (Eisen, 2008)~~IRHs) were traced semi-automatically using a ~~'maximum search'~~'maximum search'-tracking algorithm. The traveltime-to-depth conversion uses a velocity of radio waves in ice of 1.68 m/ns and includes a firn-depth correction using depth-density profiles from ice-cores collected in the area (Hubbard et al., 2013). The topographic correction and referencing to sea level is done consistently with the model geometry obtained from BedMachine Antarctica (Morlighem et al., 2020). We traced 8 internal reflection horizons (IRH1-IRH8) across the transect ~~A-A~~A–A' and 2 internal reflection horizons (IRH9-IRH10) across the transect ~~B-B~~B–B' located in Figure 1a. Along the ~~A-A~~A–A' transect, we ~~cannot trace internal reflection horizons~~ cannot trace IRHs until approximately 15 km downstream of the grounding line. This is due to a combined effect of wind erosion causing a blue ice area and a surface melt water infiltration upstream and near the grounding zone preventing formation of shallow layering ~~(Lenaerts et al., 2017)~~ (Lenaerts et al. 2017), and the CMI structure in this area where internal reflection horizons are also absent in tributary Raghnhild Ice Stream ~~(?).~~(Callens et al., 2012). Therefore, we will compare the observations with the model results from the point where the first shallow ~~internal reflection horizons~~ IRHs start to emerge within the LMI on the ice shelf.

3 Results

~~In the following, we explore the limits~~ We first explore the limitations of the approximated velocity field (MISIMP EXP1, Sect. 3.1) and quantify the degree of numerical diffusion of the age solution ~~with an analytical test case (~~(NumDiff, Sect. 3.2) ~~. We then proceed by predicting the~~ before we proceed to predict the steady-state age stratigraphy of the Roi Baudouin Ice Shelf ~~and draw out numerous characteristics which are compared to radar observations (~~(RBIS experiment, Sect. 3.3). We close by mapping the LMI/CMI boundary across the ice shelf~~.~~, and by comparing the predicted with the observed ice stratigraphy (Sect. 3.3).

3.1 ~~Assessment~~ Validation of the ~~analytical formula for vertical velocity~~kinematic forward model with full Stokes solution - MISMIP EXP1

In the ~~synthetic test case,~~MISMIP EXP1 synthetic experiment (Sect. 2.2,), the analytical approximation of the vertical velocities (Eq. 2) reproduces the full Stokes prediction with a mean deviation of 0.009 ma^{-1} (corresponding to 3 % of the total vertical velocity) for distances > 10 km away from the grounding line (Fig. 3c). Closer to the grounding-line the misfit increases with oscillating patterns reaching deviations of around $\pm$ 0.76 ma^{-1} ($\sim \pm$ 70 %) at approximately 5 km distance (Fig. 3b). Variability along the vertical axis is less than 1% throughout the shelf.

3.2 ~~Uncertainties~~ Numerical uncertainties in the predicted age-depth fields - NumDiff

Uncertainties due to numerical diffusion in the synthetic test case are highlighted in the horizontal direction using the LMI/CMI delineation line (Fig. 4a), and vertically at a cross-section near ~~x=30~~ $x = 30$ km (Fig. 4b). In both cases, the misfit between numerical and analytical solution decreases with an increase in the number of vertical layers. The mean error in the position of the delineation line decreases from $\sim$ 50 m for 10 vertical layers (vertical grid size of around 40 m) to $\sim$10 m for 200 vertical

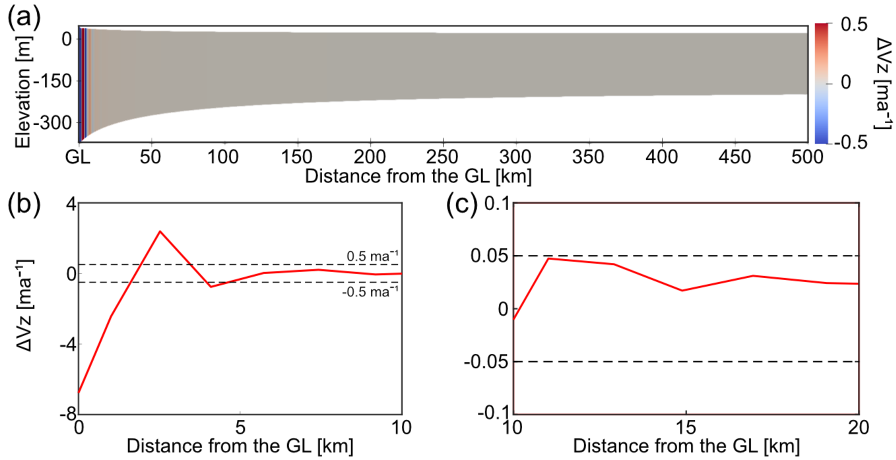

Figure 3. MISMIP EXP 1 synthetic experiment (Sect 3.1)(a) ~~Differences~~ differences between the vertical velocity calculated using Eq. (2) and the full Stokes vertical velocity obtained by Elmer/Ice~~.~~, (b) ~~Transect~~ transect values (red) from (a) for the first 10 km away from the GL and at 0 m elevation. Dashed black lines ~~represents~~ represent the $\pm$ 0.5 ma^{-1} interval~~.~~, (c) ~~Transect~~ transect values (red) from (a) between 10 km to 20 km away from the GL and at 0 m elevation. Dashed black lines ~~represents~~ represent the $\pm$ 0.05 ma^{-1} interval.

layers (vertical gridsize of around 2 m). Overall, the error is only ~~minorly~~ slightly reduced for more than 100 vertical layers. The kink in the age-depth profile is, to a certain extent, ~~smeared in~~ diffused over an approximately 25 m depth interval with the age of ice being too high in the LMI, and too low in the CMI ~~.~~ (Fig. 4b). Because of this symmetry, the deflection point of the predicted age-depth profile coincides with the LMI/CMI transition (vertical line in Fig. 4b). The extent of this diffusive zone increases with increasing simulation runtime (t_m). It is therefore necessary to minimize the simulation runtime and here this is done by choosing t_m= 300 a which corresponds to the advection time from the ~~grounding-line~~ grounding line to the ice-shelf front. Choosing longer t_m will not add more information.

Stream tracing for a fixed velocity field is not affected by the simulation runtime and reliably captures the analytical LMI/CMI transition. This will be used in the following real-world scenarios as an additional control.

3.3 ~~Modeled~~ Predicted 3D stratigraphy of the Roi Baudouin Ice Shelf - RBIS experiment

The ~~modeled~~ predicted age fields along transects ~~D1-D1~~D1–D1’ and ~~D2-D2~~D2–D2’ (located in Fig. 1a) show significant differences in the position of the LMI/CMI boundary, and the volume, between these two ice masses in the western (~~D1-D1~~D1–D1’) and eastern (~~D2-D2~~D2–D2’) part of the ice shelf (Fig. 5). In the west, the ~~D1-D1~~D1–D1’ transect mainly consists of CMI, and the position of the LMI/CMI boundary is shallow throughout the transect. We find the opposite conditions in the eastern part of the shelf, where the D2-D2’ transect is dominated by LMI, and the last 20 km leading to the terminus consists solely of LMI. This is also reflected in the deeper position of the LMI/CMI boundary throughout the transect as well as wider spacing between isochrones in the LMI. The transects D1–D1’, D2–D2’ are along straight lines, not fully following the flowline (Fig. 1a). Older ages of ice occurring in the CMI along that transect originate from the slower flowing margins containing older ice.

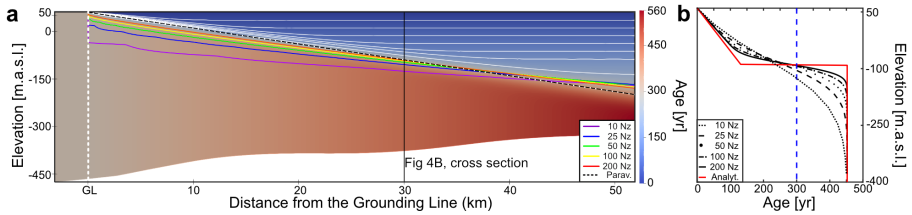

Figure 4. NumDiff experiment (Sect 3.3) (a) Modeled Age field and the delineation line between locally accumulated ice and the advected ice for a different number of vertical layers, N_z (see Legend), ~~analytically calculated delineation (white dots) and the~~ stream tracer solution from Paraview (black dashes), and analytically calculated delineation (white dots between black dashes). White lines in the LMI represent isochrones. (b) Vertical profile of the ice shelf age for different N_z at 30 km away from the grounding line. The analytical solution is represented by the red line. The blue line represents the value of the age chosen for the contours in Fig. 4a.

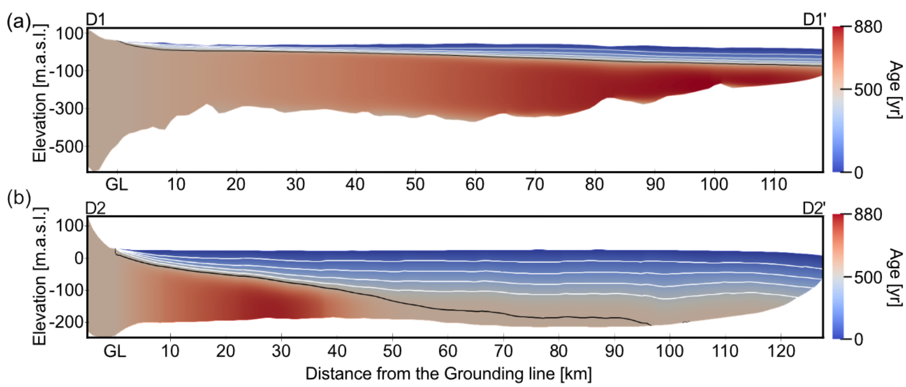

Figure 5. ~~Modeled~~ RBIS experiment, modeled age profiles along (a) D1-D1', and (b) D2-D2' profiles shown in Fig. 1a. Direction of ice flow is from left to right. White lines depict 5 isochrones at constant intervals from the surface (age = 0) to age = 450 a. The bottom isochrone (black line) in each transect approximates to the LMI/CMI boundary (age = 500 a).

Across-flow cross-sections ~~C1-C1', C2-C2' and C3-C3'~~ C1–C1', C2–C2' and C3–C3' show large variations in both the modeled age and position of the LMI/CMI boundary across each section (Fig. 6). The modeled age pattern follows the horizontal velocity field: areas with large horizontal velocities also have a shallow LMI/CMI boundary and correspondingly older ages in the CMI~~occur where horizontal velocities are large~~. Vice versa, a deeper LMI/CMI boundary and correspondingly older CMI ages occur where the ice flow is slow. Overall, the spatial extent of the LMI/CMI ratio varies greatly across the ice shelf with largest values in the eastern parts where some extensive parts are entirely sustained by LMI (Fig. 10). The western and the central parts of the ice shelf mainly consist of CMI. The inferred LMI/CMI boundary, solved using Eq.(1) are broadly consistent with the alternative approach of stream tracing from seed points located at the grounding line (Fig. 6).

In order to compare the modeled ice-shelf stratigraphy with observations, we visualize equally spaced isochrones from our predicted age field with the internal reflection horizons (IRHs) in the radar data along the transects ~~A-A~~A–A' (8 IRHs, Fig. 7) and ~~B-B~~B–B' (2 IRHs, Fig. 8). Cross-cutting of observed ~~radar~~ IRHs over modelled isochrones reflects imperfections in

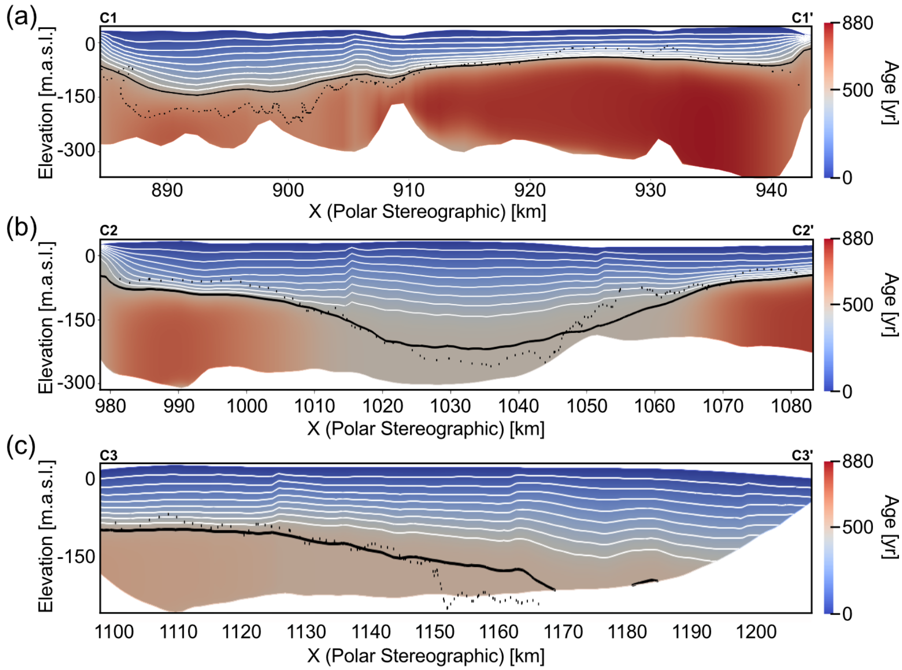

Figure 6. ~~Modeled~~ RBIS experiment, modeled age profiles along (a) ~~C1-C1'~~C1–C1', (b) ~~C2-C2'~~C2–C2', and (c) ~~C3-C3'~~ C3–C3' transects shown in Fig. 1a. Direction of ice flow is into the image. White lines depict 10 contours at constant intervals from the surface (age = 0) to age = 450 a. The bottom isochrone (black line) in each transect approximates the LMI/CMI boundary (age = 500 a). Black dots correspond to the LMI/CMI boundary calculated using stream tracing.

the model and ~~boundary conditions applied~~in the applied boundary conditions. Because the age of the ~~radar~~ IRHs is unknown, we choose the predicted ~~and observed isochrones~~ isochrones and observed IRH with similar mean depth for a one-to-one comparison (Nereson et al., 1998). Starting from the top, the predicted ages of the radar reflection horizons along transect ~~A-A~~A–A' are: 28, 45, 73, 110, 140, 175, 230 and 305 years. Across transect ~~B-B~~B–B', perpendicular to the ice flow, the predicted ~~isochrone~~ IRH ages are 20 and 100 years. ~~Furthermore, we interpolate the model age values along the observed radar isochrones, apply a moving mean, and plot the deviations of the~~ Earlier kinematic approaches use either directly modelled depth of isochrones (Arcone et al., 2005) or the age ~~of each layer from its mean value (Fig. 9).~~ field (Eisen, 2008). We follow the latter approach and obtain isochrones through contouring the finite-element age field. The predicted isochrone that is closest to the observed one in mean depth is used for comparison. Ages are also extracted at the coordinates of the observed isochrones, and the model-data misfit then corresponds to the de-meaned differences acknowledging that the age of the observed isochrone is unknown. Deviations from the mean accordingly highlight systematic misfits along the profile~~(Fig. 9).~~. Following the observed IRHs from the surface towards the bottom for ~~A-A~~A–A' (IRH1-IRH8) and ~~B-B~~B–B' transects (IRH9, IRH10), the standard age deviation for each ~~radar isochrone~~ IRH equals: IRH1~~=6.8~~: 7, IRH2~~=9.4~~: 9, IRH3~~=13.7~~: 14, IRH4~~=17.9~~: 18, IRH5~~=17.7~~: 17, IRH6~~=18.8~~: 19, IRH7~~=14.1~~: 14, IRH8~~=15.7~~: 16, IRH9~~=~~: 9 and IRH10~~=~~: 17 years.

The misfits, as exemplified by deviations from the mean age, have systematic long (> 5km)- and short (< ~~5 km~~5km) wavelength components. Close to the grounding line the predicted ages of IRHs (IRH1-IRH8) appear systematically too old, and the trend then reverses farther downstream (Fig. 9). Smaller scale deviations prominently correlate with, e.g., surface troughs in the topography. Such patterns are most likely indicative of an underressolution and systematic bias in the surface accumulation rates, but other options are also possible (Sect 4.2).

4 Discussion

4.1 ~~Advantages and shortcomings~~ Limitations of the ~~predicted age fields~~predictions and comparison to observations

Systematic mismatches between ~~predicted~~ modeled stratigraphy and observations can be attributed to multiple reasons such as (1) numerical diffusion, (2) the applied boundary conditions, (3) violation of the shallow-shelf approximation, (4) violation of the steady-state assumption, and (5) ~~flawed~~ underresolved surface accumulation or basal melt rate fields. ~~Here, we will~~ In the following, we discuss these effects separately~~in the following~~.

Numerical diffusion ~~, as shown in~~ (Fig. 4~~, is a consequence of the method used to solve~~) is inherent when solving the full advection problems, such as the age equation ~~(Eq. 1).~~ (Eq. 1; Greve et al., 2002). Increasing the vertical resolution is the best way to counterbalance this effect, and here we found that 100 vertical layers (N_z) provide a good compromise between computation runtime and loss of accuracy. Importantly, the imprint of diffusion increases with simulation runtime t_m, which is why t_m should be set to the maximum characteristic time given by the ratio of length and average velocity of the respective ice shelf. The degree of diffusion for any simulation can be quantified by comparing the LMI/CMI boundary with stream tracing which is independent of the simulation runtime. Moreover, the age solver itself can be replaced with other methods to solve the age equation~~(Born and Robinson, 2021),~~ , (e.g., Born, 2017; Born and Robinson, 2021), as the underlying host model for the velocities is simplistic and can be easily implemented in other frameworks.

The choice of a constant age value, $A(z, x = GL) = t_m$, at the inflow boundary currently precludes analysis of the radio stratigraphy in the CMI zone. In many examples, such as in our test case at RBIS or also in large parts of the McMurdo Ice Shelf (Das et al., 2020) this is acceptable, as the stratigraphy of inflowing tributary ice streams into the ice shelves is often not well preserved. Nonetheless, in areas where slow-flowing ice enters the ice shelf, the stratigraphy in the CMI may well be intact so that the boundary condition applied is unsatisfactory. In principle, this can be solved by making the inflow boundary condition one of the free parameters in the corresponding inverse problem, or use the output of a large-scale model as input for the inflow boundary of a nested ice shelf simulation.

The differences between the full Stokes Elmer/Ice vertical velocity and the analytical formula (Eq. 2) are small over the majority of the ice shelf, except within 5 km distance from the grounding line (Fig. 3), where more stress gradients are relevant than considered in ~~the shallow shelf approximation (SSA)~~SSA. More specifically, this includes an oscillating pattern that emerges at the transition between the grounded ice sheet and the floating ice shelf (Lestringant, 1994; Durand et al., 2009). Ice-shelf channel closure from lateral inflow is one example that is not adequately captured by the SSA (Drews, 2015; Wearing et al., 2021). Moreover, the surface accumulation rates likely change over these small spatial scales as discussed below. Also

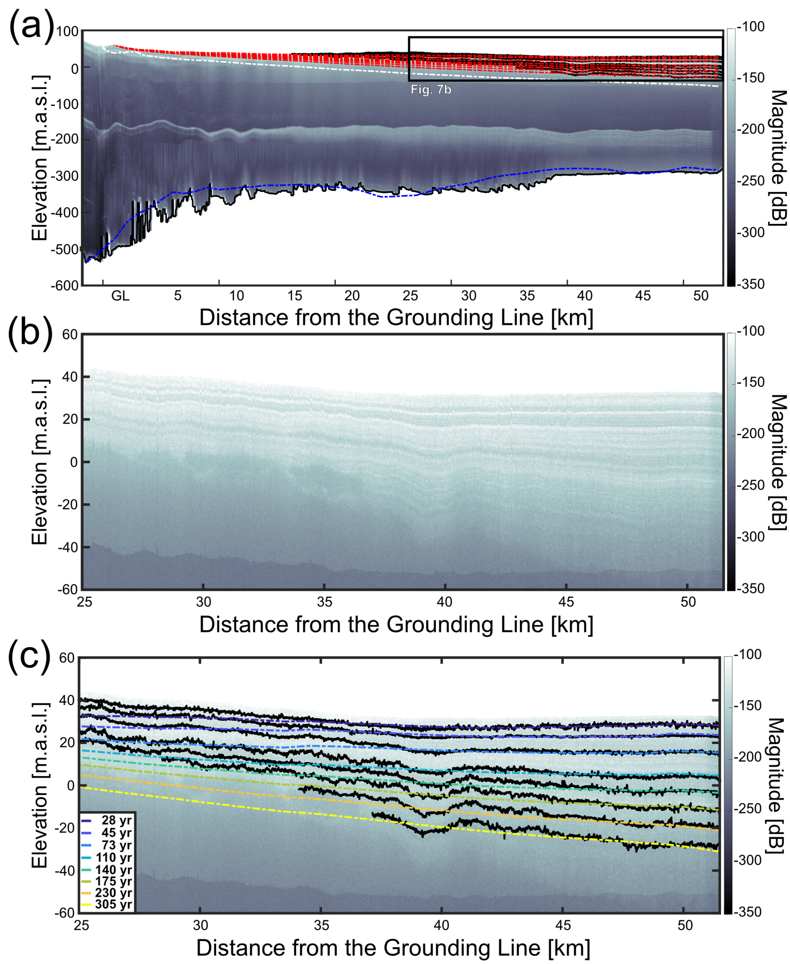

Figure 7. Comparison between radar observations and model output along ~~A-A~~A–A’ transect (located in Fig. 1a). Direction of ice flow is from left to right. (a) Radar image of the modeled ~~A-A’~~ A–A’ transect. Black lines represent digitized radar internal reflection horizons IRH1-IRH8, red lines represent modeled isochrones, and white ~~dash dot~~ dash-dotted line represents the LMI/CMI boundary. At the ice ~~shelf bottom~~shelf–ocean boundary, the blue line is the ~~ice shelf bottom~~ ice-shelf base used in the model (BedMachine Antarctica), and the black line is the ~~ice shelf~~ ice-shelf bottom picked from the radar image. Around 200 m of ~~depth~~elevation, the prominent white ~~line~~ reflection in the radar data is a multiple ~~reflection~~ from the ice surface~~and bottom~~. (b) ~~Zoomed in~~ Zoomed-in domain shown in ~~green from~~ the black rectangle in (a). Black lines are picked radar internal reflection horizons. Color dashed-dotted lines (presented in the same order as in the legend) show ~~modeled isochrones~~ predicted isochrone geometry and ~~their corresponding modeled~~ absolute ages (legend).

not included in this comparison are velocity modulations through ocean tides (e.g., Marsh et al., 2013; Rosier et al., 2017; Drews et al., 2021), although over the long timescales considered here this effect is likely to be negligible.

As the model domain starts at the grounding line, the incomplete kinematic model will predict an incorrect age profile for the shallow LMI at this location. This error will be maintained in the stratigraphy downstream. However, this effect is small

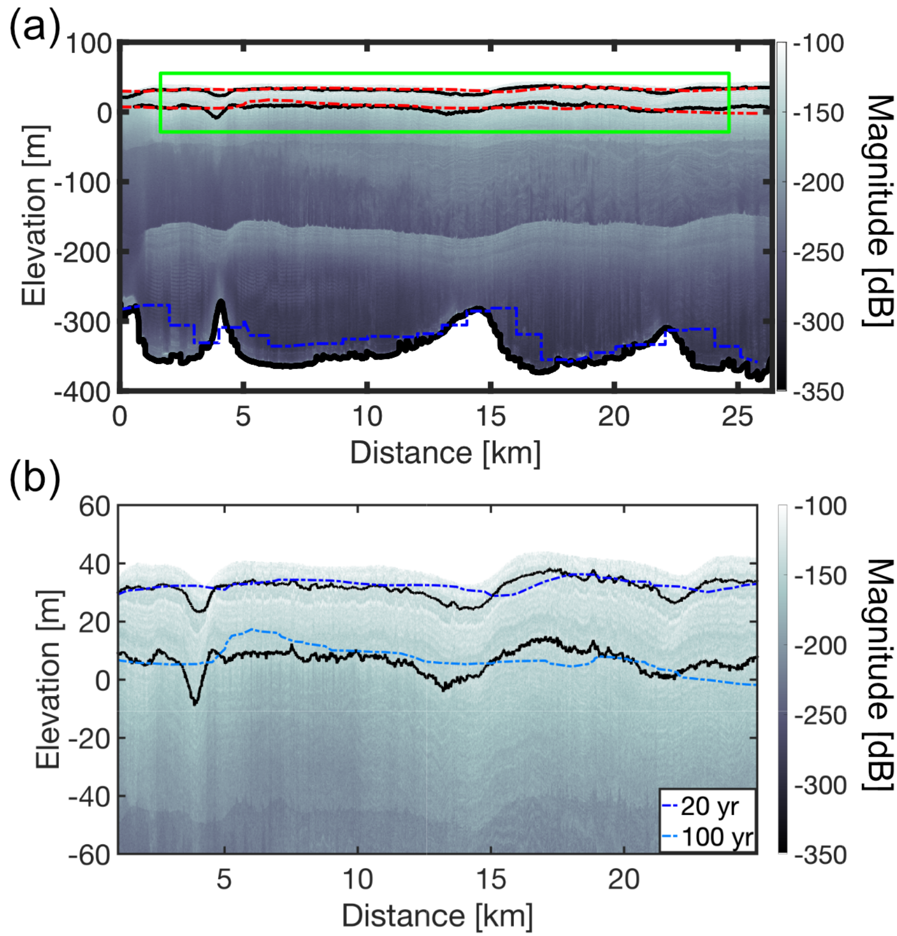

Figure 8. Comparison between radar observations and model output along ~~B-B~~B–B’ transect (located in Fig. 1a). (a) Radar image of the modeled ~~B-B~~B–B’ transect. Black lines represent picked radar internal reflection horizons IRH9 and IRH10, red lines represent modeled isochrones. At the ice ~~shelf bottom~~shelf–ocean boundary, the blue line is the ~~ice shelf bottom~~ ice-shelf base used in the model (BedMachine Antarctica), and the black line is the ~~ice shelf~~ ice-shelf bottom picked from the radar image. Around 200 m of depth, the white ~~line~~ reflection in the radar data is a multiple reflection from the ice surface~~and bottom~~. (b) ~~Zoomed in~~ Zoomed-in the domain shown in ~~green~~ the black rectangle in (a). Black lines are picked radar internal reflection horizons. ~~Dashed-dotted~~ Color dashed-dotted lines (presented in the same order as in the legend) show ~~modeled isochrones~~ predicted isochrone geometry and ~~their corresponding modeled~~ absolute ages (legend).

because (1) the missed positive and negative oscillations will, to a certain extent, average out and (2) the ice residence time (typically several tens of years) across the grounding zone is an order of magnitude smaller than the characteristic time of ice shelves (typically many hundreds of years).

The steady-state assumption in Eq. (2) can, in principle, be extended to also include transient thickness changes as observed by satellite altimetry (Paolo et al., 2015), but the kinematic model does not handle the implied change in ice geometry.

Therefore, an extension to transient cases requires more work - especially on constraining transient changes in ice geometry and velocities, as well as in atmospheric and oceanic forcings. However, a systematic mismatch between the predicted and observed stratigraphy can be treated as a first order metric that transient changes have occurred in the first place.

Given that the vertical velocities in Eq. (2) are approximately nine times more sensitive to surface accumulation rate ($\dot{a}$~~than to~~) than to basal melt rate ($\dot{b}$) (Drews et al., 2020), it is imperative to have a well-constrained ~~$\dot{a}$~~ surface accumulation field for reliable predictions of the isochronal stratigraphy. ~~Errors in the $\dot{a}$ and $\dot{b}$~~ Future temporal changes or general uncertainties in the surface accumulation and basal melt rate fields will propagate linearly into ~~a misplaced~~ changes in the position of the LMI/CMI boundary ~~. In future setups~~(Eqs. 1 and 2). If surface accumulation is well constrained and if the ice shelf is in steady-state, the forward model presented here is a step towards an inverse approach to reconstruct ~~$\dot{b}$~~ basal melt rate which is arguably least well known.

It is a logical next step to extend this method to other Antarctic ice shelves. The analysis of spatial variations of the LMI/CMI boundary across the ice shelves ~~is complementary~~ links to studies investigating ice shelf rheology and its spatial variations ~~, such as studies by Larour et al. (2005); Khazendar et al. (2011) where the authors use surface velocity observations and inverse modeling to reconstruct the viscosity field~~from inverse modeling (Larour et al., 2005; Khazendar et al., 2011). They find zones of stiffer ice and ~~less stiff ice which corresponds in parts with the presence or absence of ice advected~~ softer ice caused by the variability in ice temperature. In particular, ice from tributary ice streams ~~. This advected ice will in our case~~is colder and stiffer. In our case, this will be mapped as ~~the CMI. It appears that the inferred stiffness differences can be related to temperature differences because the CMI is characterized by colder and stiffer ice (Larour et al., 2005) than the LMI. This implies that the~~ CMI. Therefore, the spatial variations in the LMI/CMI boundary will ~~be reflected in the~~ likely reflect spatial variations of viscosity, ~~and~~ implying that ice shelves with large LMI/CMI contrast also have a large contrast in viscosity.

~~Thereby, mapping~~ Mapping and analyzing spatial variations in the LMI/CMI boundary can serve as a proxy for the sensitivity of the respective ice shelves to atmospheric or oceanographic perturbations (Levermann et al., 2020; Gilbert and Kittel, 2021). ~~Atmospheric~~ The buttressing capacity of ice shelves depends on their geometry (thickness) and structural integrity. The geometry of ice shelves dominated by LMI is hence controlled by the atmosphere, and consequently they are more susceptible to the projected changes in surface accumulation rates than ice shelves which are dominated by CMI. An atmospheric modeling study by Gilbert and Kittel (2021) ~~shows how~~ suggests that the projected future increase in surface temperature nonlinearly increases the amount, duration and extent of surface melt and runoff, which increases ~~ice shelf~~ vulnerability to hydrofracturing ~~. This impacts the structural integrity of LMI dominated areas and increases the likelihood of ice shelf disintegration, specially areas of the ice shelf~~ of ice shelves dominated by LMI. ~~Additionally, Levermann et al. (2020) project an increase of basal melt of the Antarctic ice shelves in the 21th centuary, which leads their thining, reduction of the CMI volume, and impacts the structural integrity of CMI dominated areas of the shelves~~On the other hand, ice shelves dominated by the CMI will be more susceptible to the projected increase in basal melt (Naughten et al., 2018; Levermann et al., 2020; Gilbert and Kittel, 2021).

Furthermore, the predicted isochronal field can be tested against radar observations, particularly farther seawards, where the typically well-ordered stratigraphy of the LMI occupies a larger fraction. Systematic mismatches between observations and

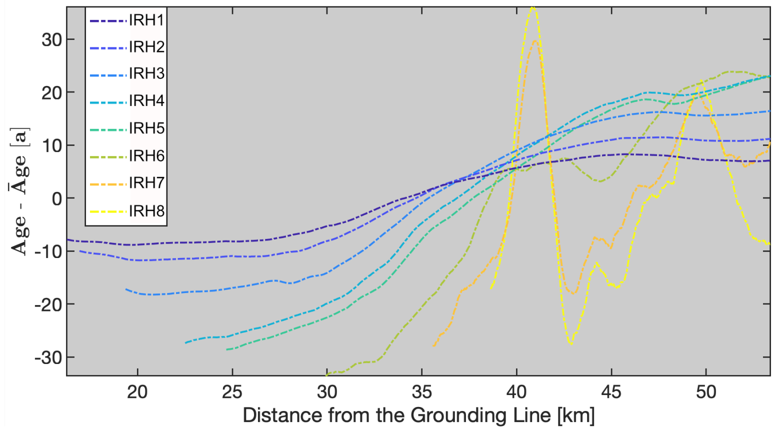

Figure 9. Modeled age deviations from picked internal reflection horizons along profiles from Figure 7, represented by lines IRH1-IRH8 starting from the surface towards the bottom.

predictions can then be discussed in terms of the forcing fields ($\dot{a}$, $\dot{b}$, V_H) and transient changes thereof. We further discuss such a comparison for the Roi Baudouin Ice Shelf.

4.2 Model-data comparison at the Roi Baudouin Ice Shelf, East Antarctica

The across- and along-flow cross-sections shown in Figs. 5 and 6 present modeled ~~expectations~~ results of the radar stratigraphy in the Roi Baudouin Ice Shelf for a given set of surface accumulation rate ($\dot{a}$) and basalt melt rate ($\dot{b}$) fields. These fields can give guidelines for the expected age-depth relationships when interpreting the stratigraphy from ice cores obtained from ice shelves (e.g., Hubbard et al., 2013). They can also be used as a planning tool for radar surveys targeting the LMI where the stratigraphy is typically more intact than in the CMI.

The comparison of ~~predicted~~ modeled isochrones with observations along ~~A-A~~A–A' captures the expected trend of a progressively increasing volume of the LMI, where the LMI/CMI boundary reaches a depth of approximately 40 m over a 50 km along-flow distance (Fig. 7a). In the radar profile, ~~internal layering only develops~~ IRHs only develop approximately 15 km downstream of the grounding line, although surface accumulation rates are positive throughout. Consequently, the model predicts formation of LMI everywhere. In this specific example, this can be explained with surface melt water infiltration in austral summers as well as with the existence of supraglacial lakes in the area upstream of the ice shelf (Stokes et al., 2019). Melt water forms at the surface due to ice-albedo feedbacks in a narrow belt near the grounding line (Lenaerts et al., 2017). This infiltration prevents the formation of a coherent radar stratigraphy even if the yearly averaged surface accumulation is positive.

Both the depth of the modeled isochrones (Figs. 7c and 8) and the age variations along the IRHs (Fig. 9) show that the modeling result better reproduces IRHs closer to the surface. Further away from the grounding line, the model results overestimate the depth of the ~~modeled isochrones~~ IRHs and do not reproduce the ~~general large scale trend until~~ large-scale trend until around the last 5 km for deeper to ~~10 km , for deeper (IRH6 - IRH8) and shallow (IRH1- IRH3) internal reflection horizons respectively (Fig. 7c). Reason for this could be due to the choice of initial condition at the grounding line (see Sect. 2.1). Assuming that~~ 15 km for shallow IRHs. Standard deviations between observations and predictions span between 7 to 19 years. Reasons for this are numerous and cannot be fully resolved here. It is possible that either the surface accumulation rates near the grounding line are too high, or that the basal melt rates are too low. For both cases (or a combination thereof), the ~~LMI starts from the present position of the grounding line , we ignore its migration in the past, which would especially impact the misfit for deeper internal radar horizons. Additional reasons could lie in the potential underestimation of basal melt in the region close to the grounding line. Figures 7c and 8 show that small scale variability , < 5 km, is not well captured, especially~~ misfits of predicted isochrones and IRHs add cumulatively over time and hence systematically increase with depth. Transient signatures in the applied fields are also a possibility and would need to be tested using inverse modeling. The same ambiguities also exist in principle for the smaller-scale variability around ice-shelf channels (Fig. 8). ~~This is unsurprising given that surface accumulation, the most important variable in predicting the stratigraphy is gridded to 5.5 km, but the surface accumulation rate likely changes on smaller spatial scales (Drews et al., 2020; Van Liefferinge et al., 2021). Figure 9 shows the offset of model ages along the observed radar isochrones, with standard deviation of age for the internal reflection horizons ranging between around 7 to 19 years, where the deviation is higher for the deeper IRHs (IRH6 - IRH8) compared to the ones close to the surface (IRH1 - IRH3). Both the depth of the modeled isochrones (Figs. 7c and 8) and the age variations along the observed radar internal reflection horizons (Fig. 9) show that the modeling result better reproduces internal reflection horizons closer to the surface.~~ However, here it is most likely that this is rather caused by an under-resolving of spatial processes in atmospheric precipitation which are known to sensitively depend on small-scale changes in surface slopes but are not yet resolved in the reanalysis data (Drews et al., 2020; Van Liefferinge et al., 2021).

~~Modeled age deviations from the mean along picked internal reflection horizons from Figure 7, represented by lines IRH1-IRH8 starting from the surface towards the bottom.~~

~~The agreement of~~ Moving further away from the grounding line, we find the comparison of model predictions and observations on larger spatial scales ~~is encouragingand provides additional evidence~~ encouraging, providing support that this particular catchment has not undergone large-scale changes in ~~the last hundreds of years~~recent time. This is in line with other studies in this area that inferred similar statements in terms of ice-dynamic stability and linked atmospheric precipitation patterns on ice rises (Drews, 2015; Callens et al., 2016). Nonetheless, whether the presented misfit is dominated by local underestimation or potential small transient changes in model forcings (surface accumulation rate, basal melt rate) is currently unclear and should be investigated in future studies.

4.3 Spatial variations in the percentage of locally accumulated ice

Mapped spatial variations show a non-uniform distribution in the percentage of LMI across the ice shelf (Figs. 5, 6 ~~&~~and 10). The differences between the western and eastern parts are reflected in the surface velocity contrast between them (Fig. 1b). Unlike the western part, where the composition of the shelf is clearly dominated by CMI advected from the Western Ragnhild

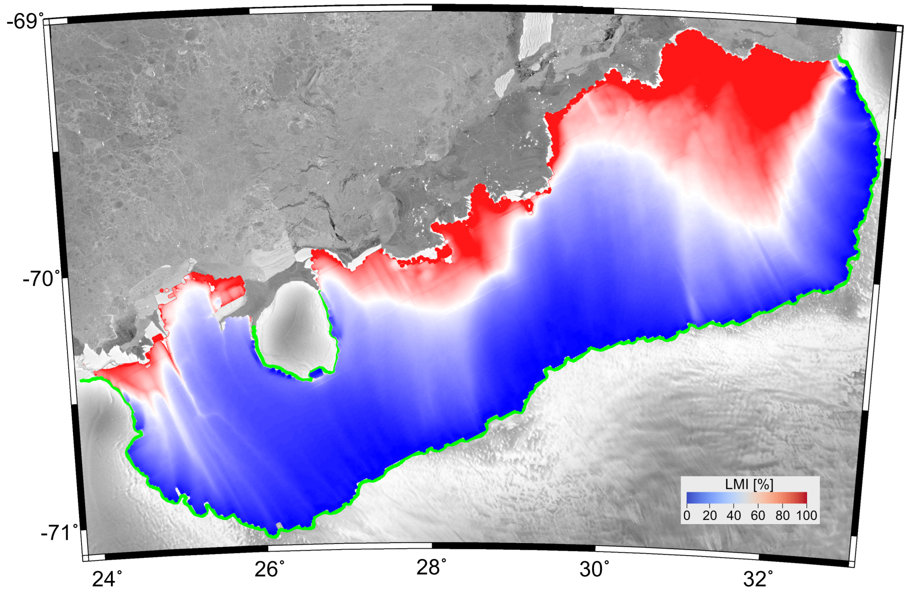

Figure 10. Percentage of local meteoric ice (LMI) over the ice shelf inferred from the steady-state age-depth fields. The white contour marks the LMI/CMI ratio of 0.5. Areas marked in red are dominated by CMI, areas in blue by LMI. The green curve represents the position of the grounding line used in the model.

Glacier, in the eastern part the total ice volume is dominated by LMI but the LMI/CMI ratio cannot be directly understood from the input data (Fig. 1).

This potentially makes the eastern part more likely to move out of close to steady-state conditions in the future, as its composition mainly depends on local surface accumulation ~~, which is predicted to decrease by year 2100 if the near-surface warming exceeds 2.5°C (Kittel et al., 2021), due to higher temperatures and increase in surface meltwater. Furthermore, this effect will be amplified by the projected increase in basal melt (Naughten et al., 2018; Levermann et al., 2020; Gilbert and Kittel, 2021) across Antarctica's ice shelves for the same period.~~ - which is prognosed to decrease (Kittel et al., 2021). Central and western areas of the shelf are less susceptible to these localized changes in mass input and output, as they mainly consist of ice accumulated on and advected from the grounded ice sheet, where future projections for the end of this century project an increase in overall surface accumulation for the +1.5°C and +2.5°C scenarios (Kittel et al., 2021).

~~Percentage of local meteoric ice (LMI) over the ice shelf inferred from the steady-state age-depth fields. Green curve represents the position of the grounding line used in the model.~~

4.4 Future development

In future applications, the analysis of the spatial variability in the LMI/CMI pattern can be expanded to give insights into its susceptibility to future changes in the atmospheric and oceanographic conditions for all ice shelves around Antarctica.

Secondly, mismatch between model output and observations can be used to refine atmospheric precipitation and ocean-induced melting on the finer spatial scale provided by the radar observations. Coupling with larger scale ice-sheet model can improve the inflow boundary condition so that also the CMI can be included in this approach.

5 Conclusions

The method here predicts the steady-state ice stratigraphy of an ice shelf using ~~observed data~~ observations (ice geometry, surface velocities, surface accumulation rate, basal melt rate) ~~combined with~~ and a simple kinematic ice-flow model. In synthetic examples, we show that the predicted vertical velocities correspond well to a full Stokes solution except in the first 5 km near the grounding line. Because the kinematic model is numerically efficient, it is possible to counterbalance numerical diffusion when solving the age equation with a high vertical resolution of 100 layers or more. Applications of this approach include calculation of the ratio between local meteoric ice (LMI) and continental meteoric ice (CMI) of ice shelves which serves as a first-order metric of the susceptibility of individual ice shelves to changes in atmospheric and oceanographic forcings. Moreover, comparing predictions with observations from radar data provides a tool to estimate whether or not, for the atmospheric and oceanographic forcing from today, the stratigraphy which typically develops over many hundreds of years is in steady state. ~~The numerical efficiency of the forward model may eventually also serve as a useful tool for the inversion of radar stratigraphy, e.g., with respect to the spatially variable basal melt rate fields.~~

The methodology is ~~exemplified~~ illustrated using the Roi Baudouin Ice Shelf in East Antarctica as a test case. The ~~most prominent model-data mismatches are due to smaller scale~~ model–observation mismatch decreases moving away from the grounding line which could be due to unresolved variability in surface accumulation rates ~~which are underresolved~~ and basal melt rates in the input data for that area. The LMI/CMI ratio of this particular ice shelf varies strongly in the east-west direction and serves as a good example for two types of endmember ice shelves that are either primarily sustained by the local surface accumulation or by the ice flux of a tributary glacier. These will respond differently should atmospheric and oceanic circulation patterns change in the near future.

Code availability. Codes for the presented examples can be found at https://github.com/vjeranv/Visnjevic_et_al_2022_TC. Elmer/Ice version 8.4 (Rev: e6ab582) used is taken from https://github.com/ElmerCSC/elmerfem. Implemented Age solver is from Martín and Gudmundsson (2012).

Author contributions. VV performed all simulations and lead writing of the manuscript. RD gave input for the study design and model setup. CS advised simulations with Elmer/Ice and optimization of the super computing environment. IK analysed the airborne radar data which were acquired by SF and DJ. All authors contributed to the writing/editing of the manuscript.

Competing interests. RD and OE are editors in The Cryosphere.

Acknowledgements. V. Višnjević, R. Drews and I. Koch were supported by an Emmy Noether Grant of the Deutsche Forschungsgemeinschaft (DR 822/3-1). CS was partially supported by the Deutsche Forschungsgemeinschaft (DFG) in the framework of the priority programme 1158 "Antarctic Research with comparative investigations in Arctic ice areas" by grant SCHA 2139/1-1. CS also acknowledges partial support by the German Federal Ministry of Education and Research (BMBF) as a Research for Sustainability initiative (FONA) through the PalMod project. S. Franke was funded by the AWI Strategy fund, D. Jansen by the AWI Strategy fund, and the Helmholtz Young investigator group HGF YIG VH-NG-802. We thank the Kenn Borek crew, and Martin Gehrmann and Sebastian Spelz of AWI's technical staff of the research aircraft Polar 6 for support on the airborne radar survey. Logistical support in Antarctica was provided at Troll Station (Norway), Novolazarewskaja-Station (Russia), and Kohnen Station (Germany). Furthermore, we acknowledge using the CReSIS toolbox generated with support from the University of Kansas, NASA Operation IceBridge grants NNX16AH54G, and NSF grants ACI-1443054, OPP-1739003, and IIS-1838230. The airborne radar data were acquired from the AWI within the CHIRP project. We thank J. Sutter and an anonymous reviewer for their helpful and constructive comments.

References

Arcone, S., Spikes, V., Hamilton, G. (2005) Stratigraphic variation within polar firn caused by differential accumulation and ice flow: Interpretation of a 400 MHz short-pulse radar profile from West Antarctica. *Journal of Glaciology*, 51(174), 407-422. doi:10.3189/172756505781829151

Adusumilli, S., Fricker, H. A., Medley, B., Padman, L., Siegfried, M. R. (2020) Interannual variations in meltwater input to the Southern Ocean from Antarctic ice shelves *Nature geoscience*, 13, 9, 616-620, https://doi.org/10.1038/s41561-020-0616-z

Alley, R.B. (1992) Flow-law hypotheses for ice-sheet modeling *Journal of Glaciology*, 38, 129, 245-256, doi:10.3189/S0022143000003658

Alley, K., Scambos, T., Siegfried, M. *et al.* (2016) Impacts of warm water on Antarctic ice shelf stability through basal channel formation *Nature Geoscience*, 9, 290–293, https://doi.org/10.1038/ngeo2675

Banwell, A. (2017) Ice-shelf stability questioned *Nature Communications*, 544, 306-307, https://doi.org/10.1038/544306a

Berger, S., Drews, R., Helm, V., Sun, S., Pattyn, F. (2017) Detecting high spatial variability of ice shelf basal mass balance, Roi Baudouin Ice Shelf, Antarctica *The Cryosphere*, 11(6), 2675-2690, https://doi.org/10.5194/tc-11-2675-2017

Bons, P., Jansen, D., Mundel, F. *et al.* (2016) Converging flow and anisotropy cause large-scale folding in Greenland's ice sheet *Nature Communications*, 7, 11427, https://doi.org/10.1038/ncomms11427

Born, A. and Robinson, A. (2017) Tracer transport in an isochronal ice-sheet model *Journal of glaciology*, 63(237), 22-38, doi:10.1017/jog.2016.111

Born, A. and Robinson, A (2021) Modeling the Greenland englacial stratigraphy. *The Cryosphere*, 15, 4539-4556, https://doi.org/10.5194/tc-15-4539-2021.

Callens, D., Drews, R., Witrant, E., Philippe, M., Pattyn, F. (2016) Temporally stable surface mass balance asymmetry across an ice rise derived from radar internal reflection horizons through inverse modeling *Journal of Glaciology*, 62, 233, 525-534, doi:10.1017/jog.2016.41

Catania, G., Hulbe, C. and Conway, H. (2010) Grounding-line basal melt rates determined using radar-derived internal stratigraphy *Journal of Glaciology*, 56(197), 545-554. doi: 10.3189/002214310792447842

CReSIS Toolbox (2020), Lawrence, Kansas, USA. Available at: https://github.com/CReSIS, https://ops.cresis.ku.edu/wiki/index.php/Main_Page

Das, I., Padman, L., Bell, R.E., Fricker, H.A., Tinto, K.J., Hulbe, C.L., Siddoway, C.S., Dhakal, T., Frearson, N.P., Mosbeux, C. and Cordero, S.I. (2020) Multidecadal Basal Melt Rates and Structure of the Ross Ice Shelf, Antarctica, Using Airborne Ice Penetrating Radar *Journal of Geophysical Research: Earth Surface*, 125, 3, https://doi.org/10.1029/2019JF005241

Drews, R. (2015) Evolution of ice-shelf channels in Antarctic ice shelves *The Cryosphere*, 9, 1169–1181, doi:10.5194/tc-9-1169-2015

Drews, R., Schannwell, C., Ehlers, T. A., Gladstone, R., Pattyn, F., Matsuoka, K. (2020) Atmospheric and oceanographic signatures in the ice shelf channel morphology of Roi Baudouin Ice Shelf, East Antarctica, inferred from radar data. *Journal of Geophysical Research: Earth Surface*, 125, 7, https://doi.org/10.1029/2020JF005587

Drews, R., Wild, C. T., Marsh, O. J., Rack, W., Ehlers, T. A., Neckel, N., Helm, V. (2021) Grounding-zone flow variability of Priestley Glacier, Antarctica, in a diurnal tidal regime. *Geophysical Research Letters*, 48, https://doi.org/10.1029/2021GL093853

Durand, G., Gagliardini, O., de Fleurian, B., Zwinger, T., Le Meur, E. (2009) Marine ice sheet dynamics: Hysteresis and neutral equilibrium *Journal of Geophysical Research*, 114, https://doi.org/10.1029/2008JF001170

Edwards, T.L., Nowicki, S., Marzeion, B. *et al.* (2020) Projected land ice contributions to twenty-first-century sea level rise. *Nature*, 593, 74-82, https://doi.org/10.1038/s41586-021-03302-y.

Eisen, O.(2008) Inference of velocity pattern from isochronous layers in firn, using an inverse method *Journal of Glaciology*, 54, 613-630, doi:10.3189/002214308786570818

Franke, S., Jansen, D., Binder, T., Dörr, N., Helm, V., Paden, J., Steinhage, D., Eisen, O. (2020) Bed topography and subglacial landforms in the onset region of the Northeast Greenland Ice Stream. *Annals of Glaciology*, 61(81), 143-153. doi:10.1017/aog.2020.12

Franke, S., Jansen, D., Binder, T., Paden, J. D., Dörr, N., Gerber, T., Miller, H., Dahl-Jensen, D., Helm, V., Steinhage, D., Weikusat, I., Wilhelms, F., and Eisen, O. (~~2021~~2022) Airborne ultra-wideband radar sounding over the shear margins and along flow lines at the onset region of the Northeast Greenland Ice Stream *Earth ~~Syst. Sci.~~ System Science Data~~Discuss. preprint~~]*, 14, 763-779, https://doi.org/10.5194/~~essd-2021-91, in review.~~ essd-14-763-2022

Fretwell, P., Pritchard, H. D., Vaughan, D. G. *et al.* (2013) Bedmap2: improved ice bed, surface and thickness datasets for Antarctica. *The Cryosphere*, 7, 375–393, https://doi.org/10.5194/tc-7-375-2013.

Fürst, J., Durand, G., Gillet-Chaulet, F. *et al.* (2016) The safety band of Antarctic ice shelves *Nature Climate Change*, 6, 479–482 (2016). https://doi.org/10.1038/nclimate2912

Gagliardini, O., Zwinger, T., Gillet-Chaulet, F., Durand, G., Favier, L., de Fleurian, B., Greve, R., Malinen, M., Martín, C., Råback, P., Ruokolainen, J., Sacchettini, M., Schäfer, M., Seddik, H., and Thies, J. (2013) Capabilities and performance of Elmer/Ice, a new-generation ice sheet mode. *Geoscientific Model Development*, 6(4), 1299–1318, https://doi.org/10.5194/gmd-6-1299-2013

Gardner, A. S., G. Moholdt, T. Scambos, M. Fahnstock, S. Ligtenberg, M. van den Broeke, and J. Nilsson (2018) Increased West Antarctic and unchanged East Antarctic ice discharge over the last 7 years *The Cryosphere*12(2), 521-547, doi:10.5194/tc-12-521-2018

Gardner, A. S., M. A. Fahnestock T. A. Scambos (2019) ITS_LIVE Regional Glacier and Ice Sheet Surface Velocities *Data archived at National Snow and Ice Data Center*, doi:10.5067/6II6VW8LLWJ7

Gilbert, E., Kittel, C. (2021) Surface Melt and Runoff on Antarctic Ice Shelves at 1.5°C, 2°C, and 4°C of Future Warming *Geophysical Research Letters*, 48(8), https://doi.org/10.1029/2020GL091733

Greve, R., Wang, Y., and Mügge, B. (2002) Comparison of numerical schemes for the solution of the advective age equation in ice sheets *Annals of Glaciology*, 35, 487–494, doi:10.3189/172756402781817112

Gudmundsson G.H. (2013) Ice-shelf buttressing and the stability of marine ice sheets *The Cryosphere*, 7, 647–655, https://doi.org/10.5194/tc-7-647-2013

Hale, R., Miller, H., Gogineni, S., Yan, J. B., Leuschen, C., Paden, J., Li, J. (2016) Multi-channel ultra-wideband radar sounder and imager. *2016 IEEE International Geoscience and Remote Sensing Symposium (IGARSS)*, 10–15 July 2016. IEEE: Beijing, China, pp. 2112–2115. https://doi.org/10.1109/IGARSS.2016.7729545.

Henderson A. (2004) The ParaView Guide. *Clifton Park, NY: Kitware*

Hindmarsh, R.C.A., Leysinger Vieli, G., Parrenin, F. (2009) A large-scale numerical model for computing isochrone geometry *Annals of Glaciology*, 50(51):130-140. doi: https://doi.org/10.3189/172756409789097450

Holschuh, N., B. R. Parizek, R. B. Alley, and S. Anandakrishnan (2017) Decoding ice sheet behav- ior using englacial layer slopes *Geophysical Research Letters*, 44, 5561–5570, doi:10.1002/2017GL073417

Hubbard, B., J.-L. Tison, M. Philippe, B. Heene, F. Pattyn, T. Malone, J. Freitag (2013) Ice shelf density reconstructed from optical televiewer borehole logging *Geophysical Research Letters*, 40, 5882–5887, doi:10.1002/2013GL058023

Jansen, D., Kulessa, B., Sammonds, P. R., Luckman, A., King, E. C. and Glasser, N. F. (2010) Present stability of the Larsen C ice shelf, Antarctic Peninsula *Journal of Glaciology*, 56(198), pp. 593–600. doi:10.3189/002214310793146223

Jansen, Daniela, M-G. Llorens, Julien Westhoff, Florian Steinbach, Sepp Kipfstuhl, Paul D. Bons, Albert Griera, Ilka Weikusat *et al.* (2016) Small-scale disturbances in the stratigraphy of the NEEM ice core: observations and numerical model simulations *The Cryosphere*, 10, 1, 359-370, https://doi.org/10.5194/tc-10-359-2016

Jenkins, A. (2016) A simple model of the ice shelf–ocean boundary layer and current *Journal of Physical Oceanography*, 46, 1785-1803, doi:10.1175/JPO-D-15-0194.1.

Jezek, K. (2003) Observing the Antarctic ice sheet using the RADARSAT-1 synthetic aperture radar. *Polar Geography*, 27(3), 197-209, https://doi.org/10.1080/789610167

Khazendar, A., Rignot, E., Larour, E. (2011) Acceleration and spatial rheology of Larsen C ice shelf, Antarctic Peninsula *Geophysical Research Letters*, 38(9), https://doi.org/10.1029/2011GL046775

Kittel, C., Amory, C., Agosta, C., Jourdain, N. C., Hofer, S., Delhasse, A., Doutreloup, S., Huot, P.-V., Lang, C., Fichefet, T., Fettweis, X. (2021) Diverging future surface mass balance between the Antarctic ice shelves and grounded ice sheet *The Cryosphere*, 15, 1215-1236, https://doi.org/10.5194/tc-15-1215-2021

Larour, E., Rignot, E., Joughin, I., Aubry, D. (2005) Rheology of the Ronne Ice Shelf, Antarctica, inferred from satellite radar interferometry data using an inverse control method *Geophysical Research Letters*, 32(5), https://doi.org/10.1029/2004GL021693

Lenaerts, J. T. M., Brown, J., Van Den Broeke, M. R., Matsuoka, K., Drews, R., Callens, D., Philippe, M., Gorodetskaya, I. V., Van Meijgaard, E., Reijmer, C. H., Pattyn, F. and Van Lipzig, N. P. M. (2014) High variability of climate and surface mass balance induced by Antarctic ice rises. *Journal of Glaciology*, 60(224), 1101-1110, doi:10.3189/2014JoG14J040

Lenaerts, J. T. M. , Lhermitte, S. , Drews, R. , Ligtenberg, S. R. M. , Berger, S. , Helm, V. , Smeets, C. J. P. P. , Broeke, M. R. v. d. , van de Berg, W. J. , van Meijgaard, E. , Eijkelboom, M. , Eisen, O. and Pattyn, F (2017) Meltwater produced by wind–albedo interaction stored in an East Antarctic ice shelf. *Nature Climate Change*, 7, 58-63, doi: 10.1038/NCLIMATE3180

Lenaerts, J. T., Medley, B., van den Broeke, M. R., Wouters, B. *et al.* (2019) Observing and modeling ice sheet surface mass balance *Reviews of Geophysics*, 57(2), 376-420, https://doi.org/10.1029/2018RG000622

Lestringant, R. (1994) A two-dimensional finite-element study of flow in the transition zone between an ice sheet and an ice shelf *Annals of Glaciology*, 20, 67-72, https://doi.org/10.3189/1994AoG20-1-67-72

Levermann, A., Winkelmann, R., Albrecht, T., Goelzer, H. *et al.* (2020) Projecting Antarctica's contribution to future sea level rise from basal ice shelf melt using linear response functions of 16 ice sheet models (LARMIP-2) *Earth System Dynamics*, 11, 35-76, https://doi.org/10.5194/esd-11-35-2020

Leysinger Vieli, G. J.-M. C., R. C. A. Hindmarsh, M. J. Siegert, and S. Bo (2011) Time-dependence of the spatial pattern of accumulation rate in East Antarctica deduced from isochronic radar layers using a 3-D numerical ice flow model *Journal of Geophysical Research*, 116, doi:10.1029/2010JF001785

Jouvet, G., Röllin, S., Sahli, H., Corcho, J., Gnägi, L., Compagno, L., Sidler, D., Schwikowski, M., Bauder, A., and Funk, M. (2020) Mapping the age of ice of Gauligletscher combining surface radionuclide contamination and ice flow modeling *The Cryosphere*, 14, 4233-4251, https://doi.org/10.5194/tc-14-4233-2020

MacAyeal, D.R. (1989) Large-scale ice flow over a viscous basal sediment: Theory and application to ice stream B, Antarctica. *Journal of Geophysical Research: Earth Surface*, 94, 4071-4087, https://doi.org/10.1029/JB094iB04p04071

Marsh, O. J., Rack, W., Floricioiu, D., Golledge, N. R., Lawson, W. (2013) Tidally induced velocity variations of the Beardmore Glacier, Antarctica, and their representation in satellite measurements of ice velocity. *The Cryosphere*, 7(5), 1375-1384, https://doi.org/10.5194/tc-7-1375-2013

Martín, C. and Gudmundsson, G. H. (2012) Effects of nonlinear rheology, temperature and anisotropy on the relationship between age and depth at ice divides. *The Cryosphere*, 6, 1221–1229, https://doi.org/10.5194/tc-6-1221-2012

Matsuoka, K., D. Power, S. Fujita, C. F. Raymond (2012) Rapid development of anisotropic ice-crystal-alignmentfabrics inferred from englacial radar polarimetry, central West Antarctica *Journal of Geophysical Research*, 117, doi:10.1029/2012JF002440

Morland, L. W. (1987) Unconfined ice-shelf flow. *Dynamics of the West Antarctic Ice Sheet*,edited by C. J. van der Veen, and J. Oerlemans, pp. 99– 116, Kluwer Acad., Dordrecht, Netherlands.

Morlighem, M., Rignot, E., Binder, T. *et al.* (2020) Deep glacial troughs and stabilizing ridges unveiled beneath the margins of the Antarctic ice sheet. *Nature Geoscience*, 13, 132-137, https://doi.org/10.1038/s41561-019-0510-8

Naughten, K. A., Meissner, K. J., Galton-Fenzi, B. K., England, M. H., Timmermann, R., Hellmer, H. H. (2018) Future projections of Antarctic ice shelf melting based on CMIP5 scenarios *Journal of Climate*, 31, 13, 5243-5261, https://doi.org/10.1175/JCLI-D-17-0854.1

Nereson, N. A., Raymond, C. F., Waddington, E. D., Jacobel, R. W. (1998) Migration of the Siple Dome ice divide, West Antarctica *Journal of Glaciology*, 44(148), pp. 643–652. doi: 10.3189/S0022143000002148

Nereson, N. A., Raymond, C. F., Jacobel, R. W., Waddington, E. D. (2000) The accumulation pattern across Siple Dome, West Antarctica, inferred from radar-detected internal layers *Journal of Glaciology*, 46(152), pp. 75–87. doi: 10.3189/172756500781833449

Nereson, N. A. and Waddington, E. D. (2002) Isochrones and isotherms beneath migrating ice divides. *Journal of Glaciology*, 48(160), pp. 95–108. doi: 10.3189/172756502781831647

Paolo, F. S., Fricker, H. A., Padman, L. (2015) Volume loss from Antarctic ice shelves is accelerating. *Science*, 348(6232), 327-331, https://doi.org/10.1126/science.aaa0940

Pattyn, F., Schoof, C., Perichon, L., Hindmarsh, R. C. A., Bueler, E., de Fleurian, B., Durand, G., Gagliardini, O., Gladstone, R., Goldberg, D., Gudmundsson, G. H., Huybrechts, P., Lee, V., Nick, F. M., Payne, A. J., Pollard, D., Rybak, O., Saito, F., and Vieli, A. (2012) Results of the Marine Ice Sheet Model Intercomparison Project, MISMIP. *The Cryosphere*, 6, 573–588, https://doi.org/10.5194/tc-6-573-2012

Pattyn, F., Matsuoka, K., Callens, D., Conway, H., Depoorter, M., Docquier, D., *et al.* (~~2021~~2012) Melting and refreezing beneath Roi Baudouin Ice Shelf (East Antarctica) inferred from radar, GPS, and ice core data *Journal of Geophysical Research*, 117, F04008. https://doi.org/10.1029/2011JF002154

Pratap B., Dey R., Matsuoka K., Moholdt G., Lindbäck K., Goel V., Laluraj C.M., Thamban M . (2021) Three-decade spatial patterns in surface mass balance of the Nivlisen Ice Shelf, central Dronning Maud Land, East Antarctica *Journal of Glaciology*, 68(267), 174-186. https://doi.org/10.1017/jog.2021.93

Rignot, E., Bamber, J., van den Broeke, M. *et al.* (2008) Recent Antarctic ice mass loss from radar interferometry and regional climate modelling *Nature Geoscience*, 1, 106–110 (2008). https://doi.org/10.1038/ngeo102

Rodriguez-Morales, F., Gogineni, S., Leuschen, C.J., Paden, J.D., Li, J., Lewis, C.C. *et al.* (2014) Advanced multifrequency radar instrumentation for polar Research *IEEE Transactions on Geoscience and Remote Sensing*, 52(5), 2824–2842. https://doi.org/10.1109/TGRS.2013.2266415

Rosier, S. H., Gudmundsson, G. H., King, M. A., Nicholls, K. W., Makinson, K., Corr, H. F. (2017) Strong tidal variations in ice flow observed across the entire Ronne Ice Shelf and adjoining ice streams. *Earth System Science Data*, 849-860, https://doi.org/10.5194/essd-9-849-2017

Schannwell, C., Cornford, S., Pollard, D., Barrand, N. E. (2021) Dynamic response of Antarctic Peninsula Ice Sheet to potential collapse of Larsen C and George VI ice shelves *The Cryosphere*, 12, 7, 2307-2326, https://doi.org/10.5194/tc-12-2307-2018

Stokes, C. R., Sanderson, J. E., Miles, B. W. J., Jamieson, S. S. R., & Leeson, A. A. (2019) Widespread distribution of supraglacial lakes around the margin of the East Antarctic Ice Sheet. *Scientific Reports*, 9(1), 13823. https://doi.org/10.1038/s41598-019-50343-5

Sutter, J., Fischer, H., Eisen, O. (2021) Investigating the internal structure of the Antarctic Ice Sheet: the utility of isochrones for spatiotemporal ice-sheet model calibration *The Cryosphere*, 15, 8, 3839-3860, https://doi.org/10.5194/tc-15-3839-2021

Thomas R.E., Negrini M., Prior D.J., Mulvaney R., Still H., Bowman M.H., Craw L., Fan S., Hubbard B., Hulbe C., Kim D., Lutz F. (2021) Microstructure and Crystallographic Preferred Orientations of an Azimuthally Oriented Ice Core from a Lateral Shear Margin: Priestley Glacier, Antarctica *Frontierss in Earth Science*, 9, 702213, https://doi.org/10.3389/feart.2021.702213

Van Liefferinge, B., Taylor, D., Tsutaki, S., Fujita, S., Gogineni, P., Kawamura, K., *et al.* (2021) Surface mass balance controlled by local surface slope in inland Antarctica: Implications for ice-sheet mass balance and Oldest Ice delineation in Dome Fuji. *Geophysical Research Letters*, 48, e2021GL094966. https://doi.org/10.1029/2021GL094966

Van Wessem, J. M., Reijmer, C. H., Morlighem, M., Mouginot, J., Rignot, E., Medley, B., Joughin, I., Wouters, B., Depoorter, M. A., Bamber, J. L., Lenaerts, J. T. M., Van De Berg, W. J., Van Den Broeke, M. R. and Van Meijgaard, E. (2014) Improved representation of East Antarctic surface mass balance in a regional atmospheric climate model. *Journal of Glaciology*, Cambridge University Press, 60, 222, pp. 761–770. doi: 10.3189/2014JoG14J051

Waddington, E. D., Neumann, T. A., Koutnik, M. R., Marshall, H.-P., Morse, D. L. (2007) Inference of accumulation-rate patterns from deep layers in glaciers and ice sheets *Journal of Glaciology*, 53, 183, pp. 694-712. doi: 10.3189/002214307784409351

Wearing, M. G., Stevens, L. A., Dutrieux, P., Kingslake, J. (2021) Ice-shelf basal melt channels stabilized by secondary flow. *Geophysical Research Letters*, 48, e2021GL094872. https://doi.org/10.1029/2021GL094872

Weis, M., R. Greve, and K. Hutter (1999) Theory of shallow ice shelves. *Continuum Mechanics and Thermodynamics*, 11, 1, 15-50, https://doi.org/10.1007/s001610050102

Winter, K., Woodward, J., Ross, N., Dunning, S.A., Hein, A.S., Westoby, M.J., Culberg, R., Marrero, S.M., Schroeder, D.M., Sugden, D.E. and Siegert, M.J. (2019) Radar-detected englacial debris in the West Antarctic Ice Sheet *Geophysical Research Letters*, 46, 17-18, 10454-10462, https://doi.org/10.1029/2019GL084012

~~, 14, 10, 3537-3550, https://doi.org/10.5194/tc-14-3537-2020~~